

PAPER • OPEN ACCESS

## Zeeman effect of isotopes of Kr and Xe investigated at the linear plasma device PSI-2

To cite this article: M Sackers *et al* 2024 *Plasma Sources Sci. Technol.* **33** 025015

View the [article online](#) for updates and enhancements.

You may also like

- [Theoretical modeling of the hybrid membrane-gas hydrate crystallisation process for xenon recovery](#)  
M S Sergeeva, A N Petukhov, M M Trubyanov *et al.*
- [Structural and vibrational properties of condensed phases in xenon molecular binary systems: He-Xe, H<sub>2</sub>-Xe](#)  
Andrew P Jephcoat, Mónica Amboage and Annette K Kleppe
- [Cross-section measurements of \(n, 2n\) and \(n, p\) reactions on <sup>124,126,128,130,131,132</sup>Xe in the 14 MeV region and theoretical calculations of their excitation functions](#)  
Junhua Luo, , Li Jiang *et al.*

**HIDEN ANALYTICAL**

# Analysis Solutions for your Plasma Research

**For Surface Science**

- ▶ Surface Analysis
- ▶ SIMS
- ▶ 3D depth Profiling
- ▶ Nanometre depth resolution

■ Compact SIMS

■ SIMS Workstation

■ Auto SIMS

**For Plasma Diagnostics**

- ▶ Plasma characterisation
- ▶ Customised systems to suit plasma Configuration
- ▶ Mass and energy analysis of plasma ions
- ▶ Characterisation of neutrals and radicals

■ ESPion

■ HPR-60 MBMS

■ EQP Series

Contact Hiden Analytical for further details:

W [www.HidenAnalytical.com](http://www.HidenAnalytical.com)  
E [info@hiden.co.uk](mailto:info@hiden.co.uk)

■ Knowledge ■ Experience ■ Expertise

[Click to view our product catalogue](#)

# Zeeman effect of isotopes of Kr and Xe investigated at the linear plasma device PSI-2

M Sackers<sup>1,\*</sup> , O Marchuk<sup>1</sup> , D Dipti<sup>2</sup> , Yu Ralchenko<sup>3</sup> , S Ertmer<sup>1</sup> , S Brezinsek<sup>1</sup>  and A Kreter<sup>1</sup> 

<sup>1</sup> Forschungszentrum Jülich GmbH, Institut für Energie- und Klimaforschung—Plasmaphysik, Partner of the Trilateral Euregio Cluster (TEC), 52425 Jülich, Germany

<sup>2</sup> International Atomic Energy Agency, Atomic and Molecular Data Unit, 1220 Vienna, Austria

<sup>3</sup> National Institute of Standards and Technology, Atomic Spectroscopy Group, Gaithersburg, MD 20899, United States of America

E-mail: [m.sackers@fz-juelich.de](mailto:m.sackers@fz-juelich.de)

Received 30 August 2023, revised 16 January 2024

Accepted for publication 30 January 2024

Published 16 February 2024



## Abstract

Laser absorption spectroscopy provides high-resolution spectra of atomic transitions that reveal many often inaccessible features. The line shapes of krypton and xenon measured in magnetized plasmas are strongly affected by the contribution of the odd-numbered isotopes <sup>83</sup>Kr, <sup>129</sup>Xe and <sup>131</sup>Xe due to their hyperfine structure, creating more challenging spectra in comparison to even-numbered ones. The lines originating from metastable levels of krypton and xenon with  $J = 2$  (Kr I 760.4 nm) and  $J = 0$  (Kr I 785.7 nm, Xe I 764.4 nm) were measured and analyzed in the linear plasma device PSI-2 in the field range of 22.5 mT–90 mT. Evaluating the Hamiltonian, including hyperfine and Zeeman interaction terms for these magnetic field strengths, unveils a deviation from the linear energy shift of the sublevels as a function of the magnetic field and from constant relative intensities that the weak field formulas provide. We prove that modeling the transitions in Xe using the weak field approximation, frequently used in magnetized plasma, becomes inadequate at  $\approx 50$  mT. In particular, the spectra of the <sup>131</sup>Xe isotope show pronounced deviations from the weak field results. For krypton, however, the situation is less critical compared to xenon due to the low natural abundance of the odd-numbered isotope.

Keywords: Zeeman effect, Magnetized plasma, Laser absorption spectroscopy, Hyperfine structure, Isotope shift, Linear plasma device

## 1. Introduction

Modeling absorption spectra obtained from atomic species in an external magnetic field requires including the Zeeman effect in the analysis [1–5]. The complexity of the spectra depends on the energy perturbation caused by the new

Hamiltonian terms compared to the fine structure (FS) energy correction terms. Usually, the splitting caused by an external magnetic field is either much smaller or larger than the FS correction. Given a small external magnetic field, first-order perturbation theory provides analytical expression to describe the energy splitting and relative intensities [6]. In magnetized plasmas with sufficient magnetic field gradients, the Zeeman pattern detected by a spectrometer can help deduce the spatial position of the atomic species emitting or absorbing the photons [7].

During the first experimental campaigns on laser absorption of metastable argon at the linear plasma device PSI-2, it sufficed to describe the spectra using simple formulas in the

\* Author to whom any correspondence should be addressed.



Original Content from this work may be used under the terms of the [Creative Commons Attribution 4.0 licence](https://creativecommons.org/licenses/by/4.0/). Any further distribution of this work must maintain attribution to the author(s) and the title of the work, journal citation and DOI.

weak field approximation (WFA) [3, 8]. Analyzing the data in this manner provided an estimate of the magnetic field strength and metastable Ar population density.

The theoretical description of the absorption spectra can be more challenging in the case of elements with multiple stable isotopes. In the case of krypton and xenon, the transition patterns increase in complexity as the gases naturally consist of several stable isotopes—three of which ( $^{83}\text{Kr}$ ,  $^{129}\text{Xe}$ ,  $^{131}\text{Xe}$ ) have a hyperfine structure (HFS). It is precisely this presence of the HFS that leads to the very complex spectra due to the interaction with a magnetic field as compared to those of a single even-numbered isotope: if the HFS splitting becomes comparable to the energy separation caused by the magnetic field, neither of the formulas available for weak or strong field limit is valid. So, for instance, the absorption spectra from  $^{133}\text{Cs}$  in neutral beam ion sources demonstrate clear examples for the Cs 852 nm line in the field range of 2.5 mT–32 mT, where the WFA is invalid as the energy splitting of the individual magnetic sublevels depends non-linearly on the external magnetic field strength [9]. The correct description requires evaluating the matrix elements of the Hamiltonian [10–12], where the HFS interaction constants are taken from experimental data or atomic structure calculations [13]. The latter approach is taken for estimating the magnetic field strength in the coronal plasma of stars [14]. An alternative method is to use a model developed by Darwin, which accounts for the magnetic dipole hyperfine interaction but neglects higher-order terms [15, 16].

The probably most relevant current research topic, where xenon and krypton spectra contain invaluable information under magnetic field strengths comparable to those investigated in this study, is spacecraft propulsion [17]. Obtaining high thrust while keeping the associated mass loss low represents a high priority. Thus, the velocity of the neutral and singly-ionized atoms is a crucial parameter accessed in the plasma plume via laser-induced fluorescence (LIF) or laser absorption spectroscopy. Typical lines accessed by the lasers are the Kr I 760.4 nm [18], Xe I 834.9 nm and Xe II 834.95 nm transitions [19–21]. For example, the Xe II line at 834.95 nm gives access to the velocity distribution function (VDF) in the plume of a Hall effect thruster at the maximal field of about 15 mT [19]. One already estimated the strong impact of the magnetic field on the derived axial velocity dispersion, but the accurate deconvolution of the line shape taking into account the Zeeman effect and HFS splitting of the odd isotopes was still not performed. In a more recent study, this deficit was removed to describe LIF spectra of the same line (Xe I 834.9 nm) up to the peak magnetic field of 65 mT in the WFA, e.g. assuming the linear Zeeman effect for the HFS components of the odd-numbered isotopes [22]. The fitting of experimental data still shows some deviations from experimental data and the modeling also indicated the presence of a significant hyperfine transition of  $^{131}\text{Xe}$  at the detuning of 5 GHz outside of the scanning range covered by the laser. In contrast to this study, the theoretical calculations demonstrated that the WFA breaks for the Xe I 834.9 nm line even at fields as low as 1.7 mT [23]. Moreover, by applying the model developed by Darwin [15, 16] and the WFA to the experimental data ( $B = 3$  mT–27 mT)

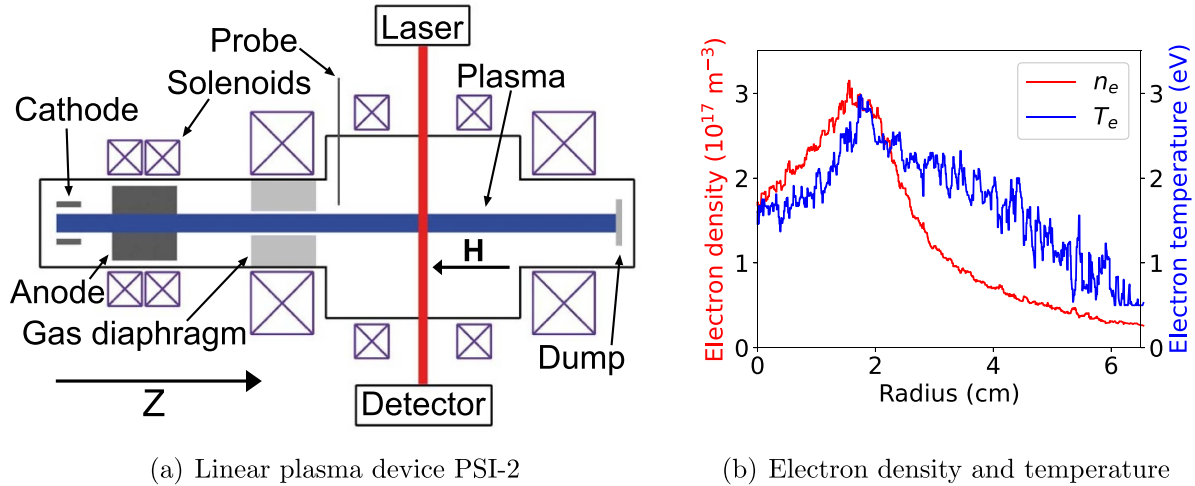
one found a difference in a gas temperature of almost a factor of two [23]. The spectral component reported in [22] at the detuning of 5 GHz for the same range of magnetic field was also not observed. The contradicting claims of [22] and [23] regarding the validity of the WFA for fields below 100 mT are one of the reasons for modeling the spectra of the Xe I line measured at the linear plasma device PSI-2.

The theoretical description of experimental data for Kr lines suffers even this level of discussion. For instance, only zero-field modeling of the Kr I 760.4 nm or Kr II 728.98 nm transitions is available in the literature [18, 24]. We are not aware of studies investigating Kr I lines in the magnetic field of tens of mT with consequent modeling taking the Zeeman effect and the HFS components into account. This work provides a detailed analysis of the absorption spectra by the Xe I 764.4 nm, Kr I 760.4 nm and 785.7 nm lines obtained at the linear plasma device PSI-2 for magnetic fields ranging from 22.5 mT–90 mT. Special attention is paid to the validity of the WFA for describing the spectral profile of Kr and Xe transitions.

The paper is structured as follows. Section 2 briefly introduces the experimental setup at the PSI-2 and presents the choice of transitions investigated in this work. Section 3 gives a brief overview of laser absorption spectroscopy. Theoretical calculations for Xe I and Kr I spectral lines observed in the experiment with and without magnetic field for odd and even isotopes are shown in section 4. Benchmarking of the model is facilitated by using the zero-, weak and strong field approximations. Section 5 shows the analysis of experimental spectra using exact calculations and the WFA. It also compares the obtained intensity of the magnetic field with the vacuum field calculations and other experimental data. Section 6 discusses the impact of spectra saturation on the line shape of Kr I lines. Finally, section 7 presents the results of the calculation and comparison with the WFA for the Xe I 834.9 nm line in the weak magnetic field.

## 2. Experimental setup

The tunable diode laser absorption spectroscopy (TDLAS) system installed at the linear plasma device PSI-2 provides the absorption spectra investigated in this work [3]. The TOPTICA DL pro diode laser covers the spectral range between 750 nm–795 nm with a linewidth of about  $\Delta\nu_L = 110$  kHz. This spectral interval allows to measure the population of metastable levels of Ar I, Kr I and Xe I atoms. Figure 1(a) presents a rough sketch of PSI-2, including the laser absorption diagnostics system. Feeding a gas into the cathode region and igniting an arc discharge towards an anode generates the plasma. A gradient in pressure drives the plasma toward the neutralization plate. The axial magnetic field  $H$  generated by six solenoids confines the particles within a radius of about 5 cm–10 cm. The overview paper [25] provides more details on the device. Tuning the current through the solenoids allows choosing a magnetic field strength of roughly 22.5 mT–90 mT along the line of sight of the TDLAS diagnostic. A Langmuir probe gives information on the plasma parameters. The profile of electron temperature and density shown in figure 1(b)



(a) Linear plasma device PSI-2

(b) Electron density and temperature

**Figure 1.** Schematic of the linear plasma device PSI-2 including the TDLAS setup and typical plasma parameters of a Kr discharge—150 A cathode current,  $8.3 \cdot 10^{-7} \text{ m}^3 \text{ s}^{-1}$  (50 sccm) Kr injected into the source, 67.5 mT and a pressure of  $4.1 \cdot 10^{-2} \text{ Pa}$ .

**Table 1.** Vacuum wavelengths, oscillator strength and configuration according to the NIST atomic spectra database [26] and the Landé splitting factors  $g$ .

Vac. wavelength (nm)	Oscillator strength	Conf. lower level	Landé $g$ lower level	Conf. upper level	Landé $g$ upper level
Kr I 760.3638	0.2368	$5s[3/2]_2^\circ$	1.502 <sup>a</sup>	$5p[3/2]_2$	1.383 71(41) <sup>b</sup>
Kr I 785.6984	0.567	$5s'[1/2]_0^\circ$	—	$5p'[1/2]_1$	1.451(1) <sup>c</sup>
Xe I 764.4128	0.56	$6s'[1/2]_0^\circ$	—	$6p'[1/2]_1$	1.551 <sup>d</sup>
Xe I 834.9116	0.73	$6s'[1/2]_1^\circ$	1.321 <sup>d</sup>	$6p'[3/2]_2$	1.190 <sup>a</sup>

 Landé  $g$  factors are taken from:

<sup>a</sup> [27]

<sup>b</sup> [28]

<sup>c</sup> [29]

<sup>d</sup> [30]

demonstrates maxima of the profiles at the distance of 2 cm from the axis of the device. The line-of-sight of the TDLAS system is at a distance of about 2 m from the hollow cathode. In the PSI-2 plasma, collisional radiative processes and diffusion determine the population density of metastable states, which the laser probes in this study. Previous work suggests that absorption by metastable atoms occurs mainly within the region that has a homogeneous magnetic field [8]. A linear polarizer enables isolating  $\pi$  ( $\Delta m = 0$ ) or  $\sigma$  ( $|\Delta m| = 1$ ) transitions, where  $m$  is the projection of the total angular momentum on the  $z$ -axis, and a set of gray filters makes it possible to probe for saturation effects, which could occur if the absorption substantially perturbs the population density of the atomic states (cf section 6).

While measuring laser absorption spectra, atomic states with substantial fractions of the overall population distribution are excellent choices for obtaining good statistics. In krypton, such a property can be expected from the ground state ( $J = 0$ ) and two metastable states in the  $4p^5 5s$  shell ( $J = 0, 2$ ) since they have no electric dipole transitions into the ground state and other multipole transitions have negligible probabilities. The quantity of light absorbed in the medium is proportional to the oscillator strength  $f_{ij}$  of the transition. Given the spectral range of the laser of 750 nm–795 nm and  $f_{ij}$ , there are

two promising candidates for absorption from the two metastable Kr I 5  $s$  levels and one line that connects to the Xe I  $6s'[1/2]_0^\circ$  level. Table 1 provides more information on their properties. The Xe I line at 834.9 nm, frequently used in LIF measurements in the Hall effect thrusters, is given here for completeness.

### 3. Tunable diode laser absorption spectroscopy at PSI-2

The fraction of light transmitted ( $T$ ) through the plasma is given by [8]

$$T(\nu) = \frac{I(\nu)}{I_0(\nu)} = \exp\left(-\int \alpha(\nu, x) dx\right), \quad (1)$$

with  $\nu$  being the photon frequency,  $I(\nu)$  the intensity of the laser light with absorption,  $I_0(\nu)$  the intensity of the laser light without absorption from atomic species present in the plasma, and  $\alpha(\nu, x)$  the coefficient of absorption. It should be justifiable to assume a constant spectral profile for volumes with significant absorption along the line-of-sight ( $\alpha(\nu, x) = \alpha(\nu)$ ), as explained in section 9.5 of [8]. In particular, the density gradient-driven transport is lower in the case of Kr and Xe due

to the higher mass as compared to Ar. The absorption coefficient depends linearly on the spectral profile [31]:

$$\alpha(\nu) \propto g(\nu) \quad (2)$$

and the main focus of this work is the influence of the magnetic field on the spectral profile  $g(\nu)$ , with

$$\int g(\nu) d\nu = 1. \quad (3)$$

All other constants and the density of the lower level are omitted from equation (2) since it is more convenient to derive the spectral profile as

$$g(\nu) = \frac{\ln\left(\frac{I(\nu)}{I_0(\nu)}\right)}{\int \ln\left(\frac{I(\nu)}{I_0(\nu)}\right) d\nu}. \quad (4)$$

Additional information on how to properly obtain  $I$  and  $I_0$  from experimental measurements are given in [8, 32].

This line profile must include all broadening mechanisms that considerably alter the spectrum. For instance, the Doppler effect of the Kr I 760.4 nm line, assuming a neutral gas temperature of 600 K (figure 8(b)), produces a broadening with a full width at half maximum (FWHM) by using equation (7.3a) of [33] of

$$\Delta\nu_D \approx 8 \times 10^{-1} \text{ GHz}. \quad (5)$$

Obviously, the laser linewidth can be neglected in the spectral analysis as  $\Delta\nu_D \gg \Delta\nu_L$ . A simple estimate of the splitting induced by the field is to use the normal Zeeman effect  $\Delta E = \mu_B H$  giving a substantial splitting for 45 mT of

$$\Delta\nu_Z \approx 6 \times 10^{-1} \text{ GHz}. \quad (6)$$

The FWHM due to the natural lifetime (equation (8.11) of [34]) of the atomic states stays below

$$\Delta\nu_N \approx 7 \times 10^{-3} \text{ GHz} \quad (7)$$

for the transitions considered in this study. We also estimated the influence of the electron-ion broadening in quasi-static approximation using the peak electron density  $3 \times 10^{17} \text{ m}^{-3}$  and temperature 3 eV of a krypton discharge, as plotted in figure 1(b). For that purpose, equation (4) of [35] provides estimates of the thermally averaged Gaunt factors of the Kr I and Xe I levels needed to calculate the width according to equation (24) of [36]. The NIST ASD [26] gives the nearest perturbing levels and the orbital quantum numbers  $l$  are 0 for the lower and 1 for the upper levels were used in [36]. Calculating this FWHM associated with the Xe I 764.4 nm line yielded the largest broadening of

$$\Delta\nu_{ei} \approx 5 \times 10^{-3} \text{ GHz}, \quad (8)$$

where the energy differences to the perturbing levels  $6p[1/2]_1$  and  $6d[5/2]_2^\circ$  used in equation (24) of [36] are  $\Delta E_i = 0.13 \text{ eV}$  and  $\Delta E_f = 0.004 \text{ eV}$ , respectively. Furthermore, isotopic effects influence the spectrum, as shown in section 4. Therefore, the only two dominant broadening mechanisms are the Zeeman and Doppler effect.

**Table 2.** Center of gravity energy shift in MHz for the six stable Kr isotopes of the transitions [38].

Transition	86–84	86–83	86–82	86–80	86–78
760.4 nm	73	94	143	221	307
785.7 nm	69	93	136	215	296

## 4. Magnetic sub-transitions of Kr I and Xe I lines: shifts and relative intensities

There are a variety of processes that may broaden or split atomic transitions. Regarding the experimental spectra in this work, isotopic effects and the interaction with an external magnetic field are dominant physical processes that need to be included in the analysis.

### 4.1. Isotopic influence on the line shape

Natural krypton and xenon consist of a variety of stable isotopes, where the differing number of neutrons in the core of the nucleus slightly shifts the center of gravity energies. The first shift is due to the difference in isotopic weight, called the mass shift and the second shift, known as the field shift, arises from the change in the charge distribution of the core [37]. For the transitions investigated in this study, sufficient literature data are available to obtain accurate wavelength shifts for different isotopes. Tables 2 and 3 present the shifts used in this work.

**4.1.1. HFS splitting.** The even-numbered isotopes of Kr and Xe have a nuclear spin  $I$  of zero and, thus, no magnetic moment associated with their core. However, the odd-numbered isotopes of Kr and Xe have nonzero nuclear spins of: [41]

- $^{83}\text{Kr } I = 9/2$
- $^{129}\text{Xe } I = 1/2$
- $^{131}\text{Xe } I = 3/2$

The orientation of the nuclear magnetic dipole to the field depends on the coupling between the angular momentum  $J$  and the spin of the nucleus  $I$ . Here, the typical rules for possible values of the new quantum number  $F = I + J$  apply [6]. This effect is known as the magnetic dipole (MD) contribution to the HFS splitting, which gives an energy correction  $E_{\text{MD}}$  of [42, 43]

$$\Delta E_{\text{MD}} = A \frac{C}{2}, \quad (9)$$

with  $A$  being the magnetic dipole HFS constant and

$$C = F(F+1) - I(I+1) - J(J+1). \quad (10)$$

Only nuclear spins greater or equal to 1 can give rise to a non-zero electric quadrupole (EQ) term, shifting the energy level in the zero-field regime by [44]

$$\Delta E_{\text{EQ}} = \frac{B}{4} \frac{3/2C(C+1) - 2I(I+1)J(J+1)}{I(2I-1)J(2J-1)}, \quad (11)$$

**Table 3.** Isotope shifts of the 764.4 nm [39] and 834.9 nm [39, 40] Xe I line compared to  $^{136}\text{Xe}$  in MHz.

Transition	136–128	136–129	136–130	136–131	136–132	136–134
764.4 nm	−274(6)	−276(9)	−202(4)	−205(12)	−150(9)	−85(6)
834.9 nm	−215.9(6.0)	−203.9(4.5)	−158.9(4.5)	−189.7(6.1)	−115.4(6.0)	−85.4(6.0)

**Table 4.** Magnetic dipole and electric quadrupole HFS constants of the atomic states taking part in the absorption process of the Kr I lines.

	$5s[3/2]_2^{\circ}$	$5s'[1/2]_0^{\circ}$	$5p[3/2]_2$	$5p'[1/2]_1$
$A_{83}$ (MHz)	−243.87(5) <sup>a</sup>	/	−108.49(12) <sup>a</sup>	226.47(16) <sup>b</sup>
$B_{83}$ (MHz)	−453.1(7) <sup>a</sup>	/	−85.7(16) <sup>a</sup>	26.5(12) <sup>b</sup>

The constants are taken from:

<sup>a</sup> [50]

<sup>b</sup> [38]

**Table 5.** Hyperfine structure constants of the levels connected to the 764.4 nm and 834.9 nm (grey-colored) Xe I transitions in MHz.

Level	$6s'[1/2]_0^{\circ}$	$6s'[1/2]_1^{\circ}$	$6p'[1/2]_1$	$6p'[3/2]_2$
$A_{129}$ (MHz)	/	−5808(2) <sup>a</sup>	1977(1) <sup>a</sup>	−2894.6(4.7) <sup>b</sup>
$A_{131}$ (MHz)	/	1709.3(7) <sup>a</sup>	−581.0(6) <sup>a</sup>	858.9(3.1) <sup>b</sup>
$B_{131}$ (MHz)	/	30.3(8) <sup>a</sup>	−6.2(4) <sup>a</sup>	−14.0(17.0) <sup>b</sup>

The constants are taken from:

<sup>a</sup> [51]

<sup>b</sup> [40]

with  $B$  being the electric quadrupole constant. Higher-order terms such as the magnetic octupole and electric hexadecapole are typically negligible [45–47].

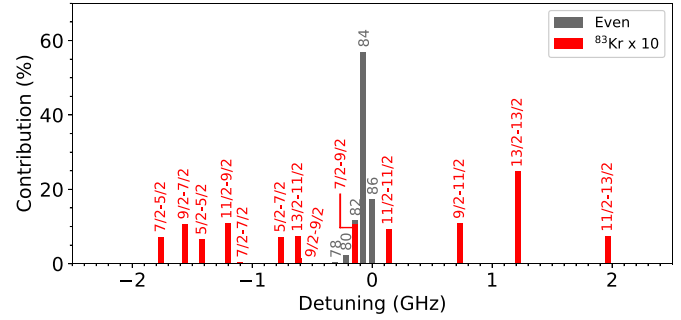
Equations (9) and (11) provide the total energy shift of the energy levels for given HFS constants without the influence of an external field. The HFS constants are given in tables 4 and 5.

Properly analyzing the line shape requires the relative intensities of the hyperfine sub-transitions. The line strength  $S_{FF'}$  of a transition from the state  $(J, F)$  to  $(J', F')$  is [48]

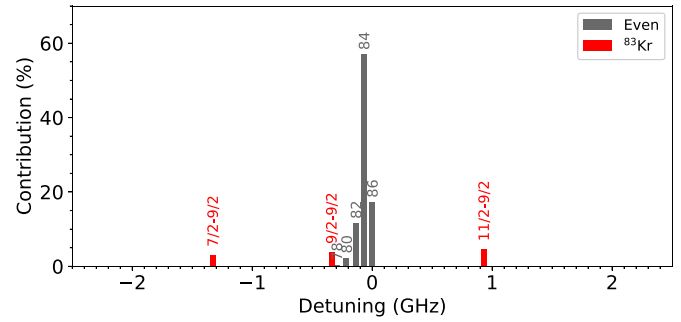
$$S_{FF'} = (2F+1)(2F'+1) \left\{ \begin{matrix} F & F' & 1 \\ J' & J & I \end{matrix} \right\}^2 S_{JJ'}, \quad (12)$$

with  $S_{JJ'}$  being the line strength of the multipole transition of the FS from the level  $J$  to the level  $J'$ . The relative intensities are calculated using the expression (12) and neglecting the factor  $S_{JJ'}$  according to [49].

Using the natural abundance of even-numbered Kr and Xe isotopes [41] and the isotope shifts (tables 2 and 3) gives the contribution of the even isotopes as plotted via the grey bars in figures 2(a), (b) and 3(a) of the lines experimentally studied in this work. Figure 3(b) shows the line at 834.9 nm of Xe I studied theoretically only. In each case, the heaviest isotope ( $^{86}\text{Kr}$ ,  $^{136}\text{Xe}$ ) is at the detuning of 0 GHz. Taking the HFS correction of the odd-numbered isotopes into account via equations (9), (11) and (12) with the values given in tables 4 and 5 yields various new components. These bars represent the zero field transition frequencies and the quantum numbers  $F$  identify the hyperfine sub-transitions.



(a) Kr I 760.4 nm



(b) Kr I 785.7 nm

**Figure 2.** Relative peak intensities of the Kr I 760.4 nm (a) and 785.7 nm (b) lines. Grey-colored bars indicate the transitions of even-numbered isotopes. The hyperfine sub-transitions of the odd isotope  $^{83}\text{Kr}$  for are shown by red bars. The intensities of the 13 transitions in  $^{83}\text{Kr}$  in (a) are multiplied by a factor of 10. The notation of the quantum numbers in the plot is according to the hyperfine sub-transitions  $F - F'$  between upper ( $F$ ) and lower level ( $F'$ ).

#### 4.2. HFS components in a magnetic field

Magnetic fields interact with the magnetic dipole moment of an atomic system and omitting the quadratic term contribute to the overall Hamiltonian as [52]

$$\mathcal{H}_{\text{mag}} = -\mu H, \quad (13)$$

where  $\mu$  is the magnetic dipole moment.

There are various regimes of the Zeeman effect that are, in principle, analogous in the cases of atoms having a fine or, additionally, a hyperfine structure. For instance, the Hamiltonian used as a perturbation for atoms in an external magnetic field with hyperfine interaction terms is [34, 43]

$$\mathcal{H} = A\mathbf{I} \cdot \mathbf{J} + B \frac{3(\mathbf{I} \cdot \mathbf{J})^2 + \frac{3}{2}(\mathbf{I} \cdot \mathbf{J}) - I(I+1)J(J+1)}{2I(2I-1)J(2J-1)} + g_J \mu_B \mathbf{J} \cdot \mathbf{H} - g_I \mu_N \mathbf{I} \cdot \mathbf{H}, \quad (14)$$

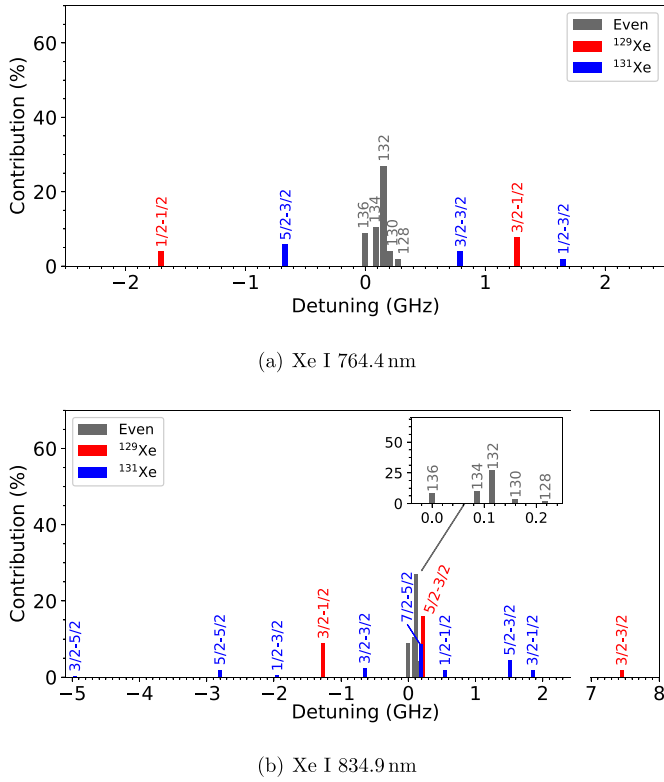


**Figure 3.** Relative peak intensities of the Xe I 764.4 nm (a) and 834.9 nm (b) lines. Grey-colored bars indicate the transitions of even-numbered isotopes. The hyperfine sub-transitions in the odd isotope  $^{129}\text{Xe}$  are shown in red and transitions in the isotope  $^{131}\text{Xe}$  in blue. Summing up the contributions given by the red or the blue bars gives the natural abundance of  $^{129}\text{Xe}$  or  $^{131}\text{Xe}$ , respectively.

with  $g_I$  being the  $g$ -factor associated with the nuclear magnetic dipole moment  $\mu_N$  [53].

Appendix shows the derivation of the formula needed to calculate the relative intensities for given expansion coefficients. In most cases, it suffices to use analytical expressions derived from the Hamiltonian (14) for the two limiting cases of the interaction of the atomic system with an external magnetic field. These situations arise if the terms depending on the magnetic field strength dominate the Hamiltonian or the hyperfine interaction is much larger. In any other case, the correct treatment requires evaluating the matrix elements.

**4.2.1. Weak field limit—WFA.** If the level splitting induced by the magnetic field is much smaller than the FS/HFS splitting, it is possible to derive the linear shift of the energy eigenvalue

$$\Delta E = gm\mu_B H, \quad (15)$$

where  $m$  denotes the magnetic quantum number,  $\mu_B$  is the Bohr magneton and  $g$  is the Landé splitting factor [42]:

$$g = \begin{cases} \text{FS} & \\ \text{HFS} & g_F \approx g_J \frac{F(F+1)+J(J+1)-I(I+1)}{2F(F+1)}. \end{cases} \quad (16)$$

The additional factor in the case of the HFS Landé splitting factor results from the vector coupling of  $I$  with  $J$ , forming the new quantum number  $F$ . Thus, there is a projection of the magnetic moment associated with  $J$  onto  $F$ . Analogously, the tiny magnetic moment of  $I$  slightly shifts the splitting factor but is generally insignificant.

The relative intensities of the magnetic sub-transitions are [6]

$$I \propto \begin{cases} \text{FS} & \left( \begin{array}{ccc} J & 1 & J' \\ -m_J & m_J - m_{J'} & m_{J'} \end{array} \right)^2 \\ \text{HFS} & \left( \begin{array}{ccc} F & 1 & F' \\ -m_F & m_F - m_{F'} & m_{F'} \end{array} \right)^2, \end{cases} \quad (17)$$

where allowed transitions satisfy  $|\Delta m| \leq 1$ .

**4.2.2. Strong field regime.** For fields where the interaction with the magnetic field dominates the contribution to the Hamiltonian (14) as compared to the FS/HFS splitting, an independent precession of the decoupled vectors about the magnetic field lines becomes apparent—see, for instance, [54].

The electric dipole operator acts upon the spatial part of the wave function and not upon the spin of the electrons or the spin of the core and thus, the selection rules for the magnetic quantum numbers are in the FS case [6]

$$\Delta m_L = \pm 0, 1 \quad (18)$$

$$\Delta m_S = 0 \quad (19)$$

and analogously in the HFS case [42]

$$\Delta m_J = \pm 0, 1 \quad (20)$$

$$\Delta m_I = 0. \quad (21)$$

Here,  $m_L$  is the projection of the orbital quantum number  $L$ ,  $m_S$  is the projection of the spin  $S$  and  $m_I$  is the projection of the nuclear momentum  $I$  on the direction of the magnetic field, e.g. the  $z$ -axis.

According to first-order perturbation theory, the energy shift for atoms with a nonzero nuclear magnetic moment in a strong field is [34, 55]

$$\Delta E = Am_J m_I + B \frac{[3m_J^2 - J(J+1)][3m_I^2 - I(I+1)]}{4I(2I-1)J(2J-1)} + m_J g_J \mu_B H - m_I g_I \mu_N H. \quad (22)$$

The structure is essentially the same as for the weak field regime of the FS case since the term  $m_J g_J \mu_B H$  dominates the energy shift of equation (22). In general, there are  $2I+1$  components of equal intensity underneath each magnetic sub-transition of the FS due to equation (21) [56].

**4.2.3. Comparison of the WFA with the exact solution.** The Wigner 3- $j$  symbol of equations (17) and (A.6) gives nonzero relative intensities only if the difference in magnetic quantum numbers  $m_{J'} - m_J$ , is  $-1, 0$ , or  $1$ . These values correspond to

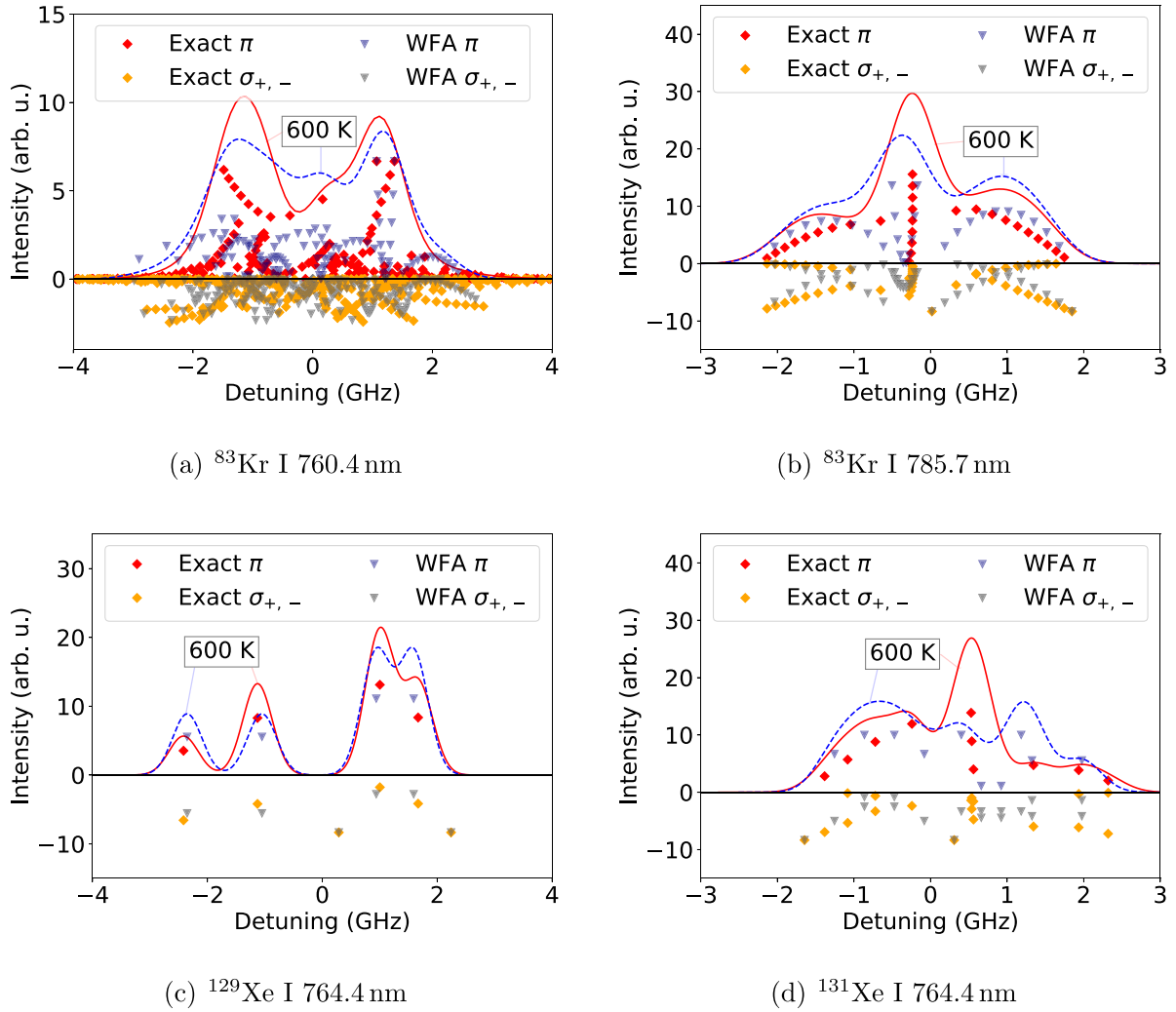


**Figure 4.** Weak field approximation (WFA) patterns of odd-numbered Xe and Kr isotopes for the three transitions experimentally investigated in this study compared to the exact solution assuming a magnetic field of 45 mT. These calculations include the isotope shift relative to the heaviest one ( $^{83}\text{Kr}$ ,  $^{136}\text{Kr}$ ). The solid red-colored (exact) and dashed blue-colored (WFA) lines are synthetic spectra of the  $\pi$  components at a neutral gas temperature of 600 K (cf figure 8(b)).

several polarization of the light. Those with  $\Delta m = 0$  are linearly polarized parallel to the magnetic field line direction ( $\pi$ ), whereas those with  $\Delta m = -1$  ( $\sigma_-$ ) and  $\Delta m = +1$  ( $\sigma_+$ ) are circularly polarized in the plane perpendicular to the magnetic field lines. The following sum rule holds true for the line of sight perpendicular to the magnetic field direction [43]

$$\sum I_{\pi} = \sum I_{\sigma}, \quad (23)$$

as verified by the absorption measurements on metastable argon [8].

Obtaining the correct energy splitting and relative intensities using WFA formulas is essentially a two-step procedure: Firstly, the zero-field splitting is calculated, as shown by the red bars in figure 2(a), via equations (9), (11), and (12). Secondly, each hyperfine sub-transition splits into its weak field pattern, where equations (15) and (16) give the energy splitting, and equation (17) provides their relative intensities.

The exact solution in the presence of magnetic field relies on calculating the energy eigenvalues and expansion coefficients by diagonalizing the Hamiltonian (14). We performed this in the basis of  $|Im_J m_J\rangle$  wavefunctions. The matrix elements of the  $(\mathbf{I} \cdot \mathbf{J})$  operator were calculated using the standard expression for the step-up and step-down operators [49], alternatively they can be calculated using equation (3) of section 7.3 [49]. The diagonalization was performed using the SciPy v.1.11.4 (scipy.linalg) package. The relative intensities of hyperfine sub-components are obtained using the expansion coefficients and equation (A.6) given in the appendix. In all cases, we ensured that evaluating the Hamiltonian (14) provides the weak field solutions for fields  $\ll 45$  mT (section 4.2.1) and the strong field pattern for fields  $\gg 45$  mT (section 4.2.2).

Figures 4(a)–(d) present the splitting and relative intensities of the lines associated with the odd-numbered isotopes of Kr and Xe for a magnetic field of 45 mT. The intensities of  $\pi$  ( $\Delta m = 0$ ) transitions are shown with positive signs, whereas

those of  $\sigma$  ( $\Delta m = \pm 1$ ) components are plotted with negative signs in accordance with the usual representation [6].

The number of magnetic sub-transitions of the exact solution and WFA is identical for figures 4(b)–(d) but differs substantially in figure 4(a). The WFA formulas applied to the Kr I 760.4 nm line give 356 possible transitions, where each component contributes more than 0.002% to the overall spectrum. However, using the exact approach of evaluating the Hamiltonians (14) gives 502 of the in total 620 possible components that surpass a contribution of 0.002% for a magnetic field of 45 mT.

One can understand this behavior by considering the following:  $F = I + J$  and  $m_F$  are good quantum numbers for weak fields. E1 transitions of nonzero intensity require  $|\Delta F| \leq 1$  and  $|\Delta m_F| \leq 1$ . Increasing the field strength provides mixing of magnetic sublevels with the same total magnetic quantum number  $m_F$  but differing  $F$  ( $F$  is not a good quantum number any more). Thus, the magnetic field induces transitions between levels with  $|\Delta F| > 1$  and  $|\Delta m_F| \leq 1$ , increasing the overall number of lines with nonzero intensity, which is precisely the reason for the large number of additional components plotted in figure 4(a). Further increase of the magnetic field reduces the number of components again since the complete decoupling of  $I$  and  $J$  leads to a strong field pattern (the Paschen-Back effect) with 120 nonzero components, which is  $2I + 1$  times the number of FS magnetic sub-transitions according to selection rules (21) and (20), respectively.

The patterns plotted in figures 4(b)–(d) are special cases since the lower level consists only of the state  $F = I$  due to  $J = 0$ , while there are three upper levels ( $F \in \{I - 1, I, I + 1\}$ ). Thus, increasing the field does not increase the number of transitions but solely redistributes the relative intensities. Laser absorption measurements of spectra of Ar at PSI-2 suggest a temperature of neutral Kr and Xe to be around 600 K for this field strength. Resulting profiles of the  $\pi$  component obtained by convolution of the Doppler profile for the calculated magnetic sub-transitions are also plotted in figures 4(a)–(d). Both curves exemplify an agreement between the WFA and exact calculations. So, for instance, despite a significant difference in the distribution of intensities of the spectral lines at 760.4 nm and 785.7 nm for  $^{83}\text{Kr}$ , the deviation between the two curves is observed only on the level of 20%–30%. In the case of Xe isotopes, the difference in line shape is much more pronounced for the  $^{131}\text{Xe}$  I 764.4 nm line compared to  $^{129}\text{Xe}$ . The deviation between the curves exceeds 50% in the frequency range of 0.6 GHz–2 GHz. For the  $^{129}\text{Xe}$  isotope, the deviation between the WFA and exact calculations remains on the order of 20% again.

A common approach for making an initial guess whether weak field or strong field formulas apply is to calculate the ratio [43]

$$\epsilon = \left| \frac{g_J \mu_B H}{A} \right|. \quad (24)$$

So, for instance, if the magnetic field strength creates a frequency shift orders of magnitude smaller than the hyperfine

**Table 6.** Ratio of the Zeeman interaction term to the MD contribution for Kr I levels at 45 mT.

	$5s[3/2]_2^\circ$	$5s'[1/2]_0^\circ$	$5p[3/2]_2$	$5p'[1/2]_1$
$\epsilon_{83}$	3.9	/	8.0	4.0

**Table 7.** Ratio of the contribution by the Zeeman effect to the MD hyperfine interaction by Xe I levels at 45 mT.

Level	$6s'[1/2]_0^\circ$	$6s'[1/2]_1^\circ$	$6p'[1/2]_1$	$6p'[3/2]_2$
$\epsilon_{129}$	/	0.14	0.49	0.26
$\epsilon_{131}$	/	0.49	1.68	0.87

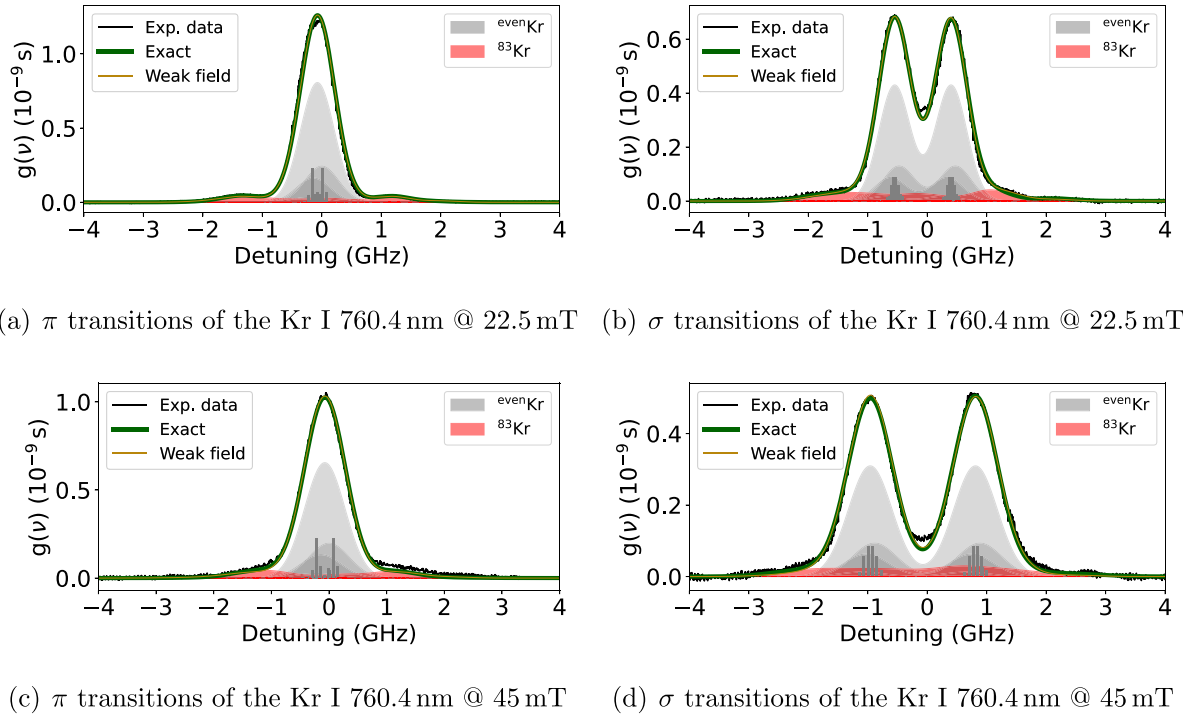
splitting due to the magnetic dipole interaction ( $\epsilon \ll 1$ ), the WFA works. In the inverse case—the Zeeman splitting is much larger ( $\epsilon \gg 1$ )—the strong field formulas are valid. Tables 6 and 7 show these ratios for a magnetic field of 45 mT. For instance, the value of 4.0 for the Kr I  $5p'[1/2]_1$  state indicates that strong field formulas should work better since the contribution by the external magnetic field surpasses the MD hyperfine interaction term in the Hamiltonian (14). However, this ratio neglects the EQ interaction, the detailed structure of the atomic level, and that Zeeman and hyperfine interaction terms can contribute to the same matrix elements. Both the weak field and strong field formulas produce symmetric patterns around their zero-field position. Undoubtedly, figures 4(a) and (d) present patterns that do not exhibit such symmetry, but figures 4(b) and (c) approximately resemble the weak field pattern. Thus, we only compare the spectra produced by the WFA to those derived using the exact approach.

The ratios of hyperfine to Zeeman contribution for 45 mT in the case of the Xe I levels show that weak field and strong field formulas probably do not apply either. Essentially, the ratio is neither large nor small enough to motivate using weak or strong field formulas but, instead, requires evaluating the Hamiltonians (14).

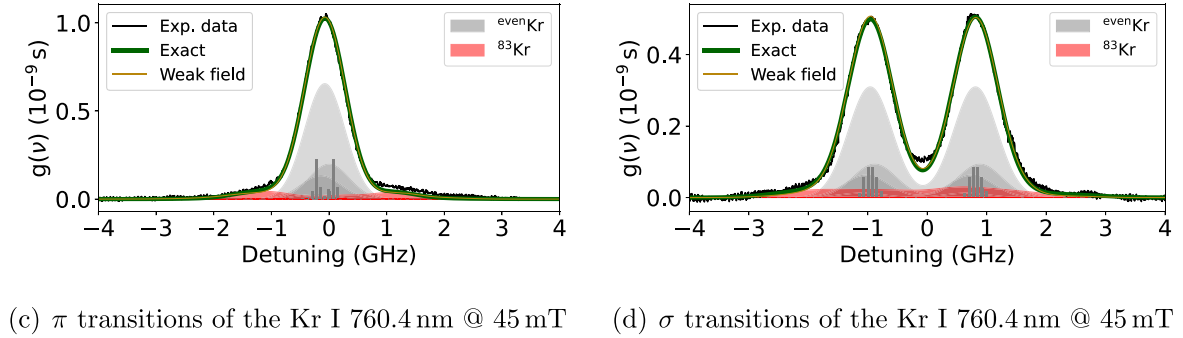
## 5. Analysis of experimental spectra

The experimental spectra are fitted using three parameters. They are the normalization constant, the temperature of the Gaussian profile and the magnetic field strength. Each isotope contributes to the total spectra according to their natural abundance [41], and the WFA formulas of section 4.2.1 apply to all even-numbered isotopes. Calculating the spectra of odd-numbered isotopes was discussed in the previous section. The spectra shown in the following section were measured by rotating a linear polarizer parallel to the field direction to measure absorption by  $\pi$  components, whereas rotating the linear polarizer by 90 degrees allowed measuring absorption by  $\sigma$  transitions.

Figures 5(a)–(d) and 6(a)–(d) show the line profile measured by laser absorption from both Kr I lines of  $\pi$  and  $\sigma$  transitions for an external magnetic field of 22.5 mT and 45 mT. An overall excellent agreement is obtained between the measured



(a)  $\pi$  transitions of the Kr I 760.4 nm @ 22.5 mT (b)  $\sigma$  transitions of the Kr I 760.4 nm @ 22.5 mT



(c)  $\pi$  transitions of the Kr I 760.4 nm @ 45 mT (d)  $\sigma$  transitions of the Kr I 760.4 nm @ 45 mT

**Figure 5.** Experimentally measured line profiles of the 760.4 nm Kr I line for magnetic fields of 22.5 mT and 45 mT compared to modeling. Rotating a linear polarizer allowed access to  $\pi$  and  $\sigma$  transitions. The grey-colored bars represent the magnetic subtransitions of the even isotopes calculated using the WFA. Convoluting these with a Gaussian profile gives five grey-shaded curves representing the contributions of the isotopes  $^{78}\text{Kr}$ ,  $^{80}\text{Kr}$ ,  $^{82}\text{Kr}$ ,  $^{84}\text{Kr}$  and  $^{86}\text{Kr}$  to the total fit. For  $^{83}\text{Kr}$ , the exact approach of evaluating the Hamiltonian provides the line positions and relative intensities. The red-shaded curve illustrates the contribution of  $^{83}\text{Kr}$  to the total spectrum, which is the sum of even and odd isotopes (green solid line). Applying the weak field formulas to  $^{83}\text{Kr}$  gives a slightly different fit, shown as the golden-colored line.

and simulated data. The parameters are fitted as follows. The energy splitting between the corresponding  $\sigma_-$  ( $\Delta m = -1$ ) and  $\sigma_+$  ( $\Delta m = +1$ ) transitions depends significantly on the magnetic field strength—in the WFA linearly. For example, there are two distinct peaks in figures 5(b) and (d), whose frequency offset depends on the field strength. Consequently, these spectra are an excellent choice for deriving the temperature and the magnetic field strength. The green line represents the total fit of all isotopes that treat the  $^{83}\text{Kr}$  isotope by evaluating the Hamiltonians (14), whereas the golden-colored line represents the WFA using the temperature and field strength derived from the exact solution. The grey-colored bars indicate the magnetic sub-transitions of the even-numbered isotopes for the field strength derived from the fit. Each grey-shaded curve gives the overall contribution of these isotopes. The red bars and red curves correspond to absorption by  $^{83}\text{Kr}$  using the exact treatment, forming additional broad wings of the spectra. Using the rigorous method gives slightly better fits than when applying WFA formulas to all isotopes.

The  $\pi$  transitions shown in figures 5(a) and 6(a) do not depend sufficiently on the magnetic field strength to infer its value. Thus, the field strength derived from fitting the  $\sigma$  components is fixed, while the temperature of the Gaussian is a free parameter in the fit of  $\pi$  spectra. We point out that the natural abundance of  $^{83}\text{Kr}$  is only 11.5%, so even-numbered

isotopes dominate the spectrum and cover up a large part of the spectrum induced by  $^{83}\text{Kr}$ .

The absorption spectra by the Xe I 764.4 nm line presented in figures 7(a)–(d) show substantially more changes in the line profile when varying the field strength. This behavior occurs since the natural abundance of odd-numbered isotopes of xenon is almost 50%. One feature is that the  $\pi$  spectra depend noticeably on the magnetic field strength through the odd-numbered isotopes, whereas the line profile associated with the even-numbered isotopes of the  $J = 1 - J = 0$  transition depends only on the temperature. Thus, the magnetic field strength and temperature are free parameters in the fits of both and the  $\pi$  and the  $\sigma$  transitions of the xenon line for external magnetic fields of 22.5 mT and 45 mT. Both parameters are the input into the simulations using purely the WFA formulas. Also, in this case, one obtains the spectra being in reasonable agreement with the experimental ones at 22.5 mT. Further increasing the field to 45 mT indicates that these WFA formulas rapidly cease to be valid, as figure 7(c) shows. For instance, the composite  $\pi$  spectrum of the  $^{131}\text{Xe}$   $[3/2 - 3/2]$ ,  $^{129}\text{Xe}$   $[3/2 - 1/2]$  and  $^{131}\text{Xe}$   $[1/2 - 3/2]$  hyperfine sub-transitions (cf figures 3(a) and 4(c)–(d)) at around 0.6 GHz–2 GHz indicate rather large deviations of the WFA formulas to the rigorous approach. The experimental spectrum supports this finding. Likewise, a pronounced asymmetry develops for the  $\sigma$

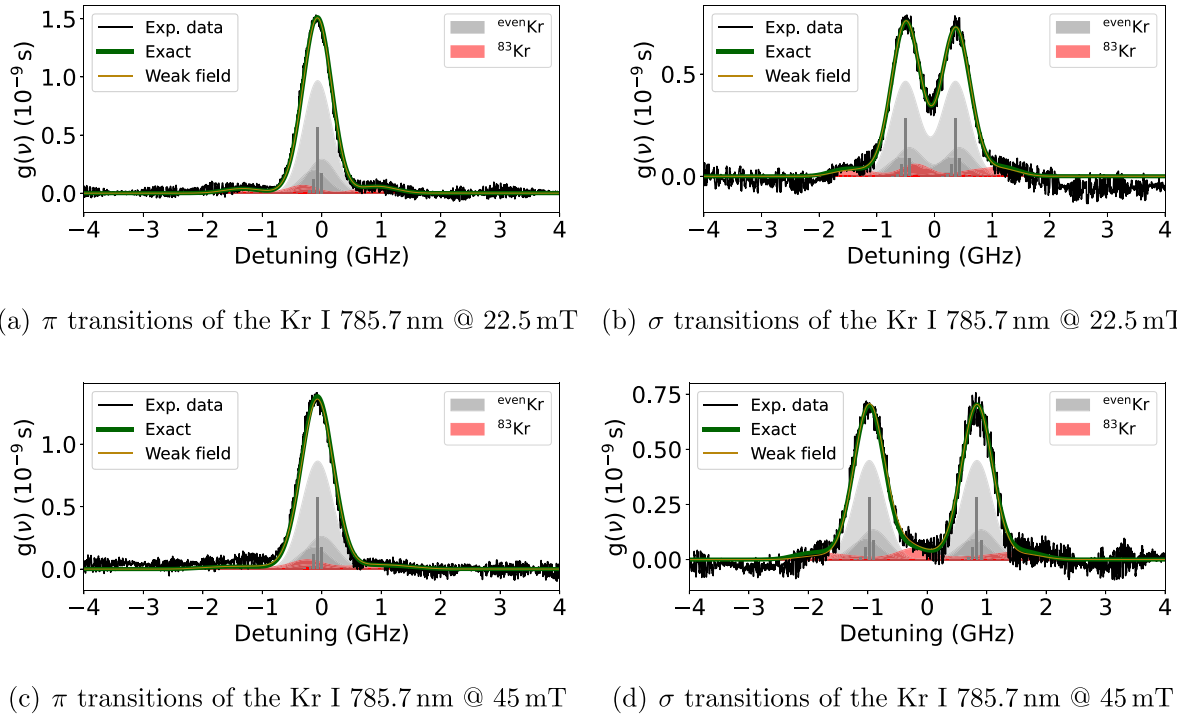


**Figure 6.** Experimental data for  $\pi$  (a), (c) and  $\sigma$  (b), (d) transitions measured using rotated linear polarizer are shown using black line. The grey-colored bars represent the magnetic subtransitions of the even isotopes calculated using the WFA. The five grey-shaded curves give contributions of the isotopes  $^{78}\text{Kr}$ ,  $^{80}\text{Kr}$ ,  $^{82}\text{Kr}$ ,  $^{84}\text{Kr}$  and  $^{86}\text{Kr}$  to the total fit using Gaussian profiles. For  $^{83}\text{Kr}$ , the exact approach of evaluating the Hamiltonian provides the line positions and relative intensities. The red-shaded curve illustrates the contribution of  $^{83}\text{Kr}$  to the total spectrum, which is the sum of even and odd isotopes (green solid line). Applying the weak field formulas to  $^{83}\text{Kr}$  gives a slightly different fit, shown as the golden-colored line.

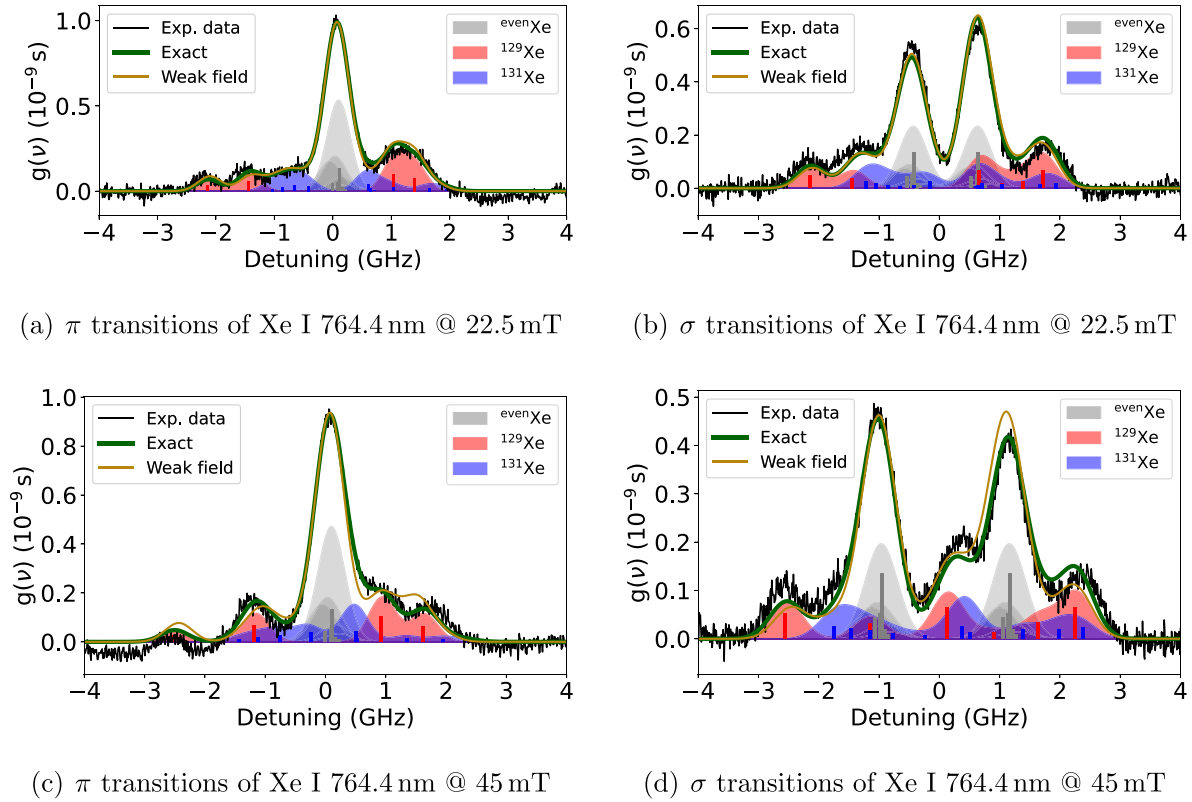
component at 1 GHz of figure 7(d), which the exact approach captures, but the WFA formulas fail to describe accurately.

The magnetic field strengths obtained from fitting the Kr I and Xe I spectra are compared to vacuum field calculations since the plasma pressure is much lower than the magnetic pressure. The magnetic field generated by the six solenoids is calculated numerically using the axial symmetry of the linear plasma device PSI-2 [57]. Hall probe measurements performed along the line of sight used by the laser diagnostic verified the vacuum field calculations. Figure 8(a) depicts the magnetic field, as per numerical calculation, and the field obtained by analyzing experimental data. Here, an error of about 5% is assumed for the vacuum field due to some uncertainties in the position of the solenoids and the exact optical path of the light emitted by the laser through the vacuum vessel. Hall probe measurements along the line of sight used by the laser confirm the vacuum field calculation and the point shown in figure 8(b) corresponds to  $r=0$ . Figure 22 of [8] compares the Hall probe measurements to the Biot–Savart law for  $r \neq 0$ . The diamonds and stars represent the results obtained by analyzing the absorption spectra from Kr. They agree remarkably well with the theoretical estimation for fields from 22.5 mT–90 mT. As predicted, the  $\pi$  transitions of the Xe I line depend sufficiently on the field strength to derive adequate values from fitting these spectra. Absorption spectra by metastable argon states indicated a systematically lower magnetic

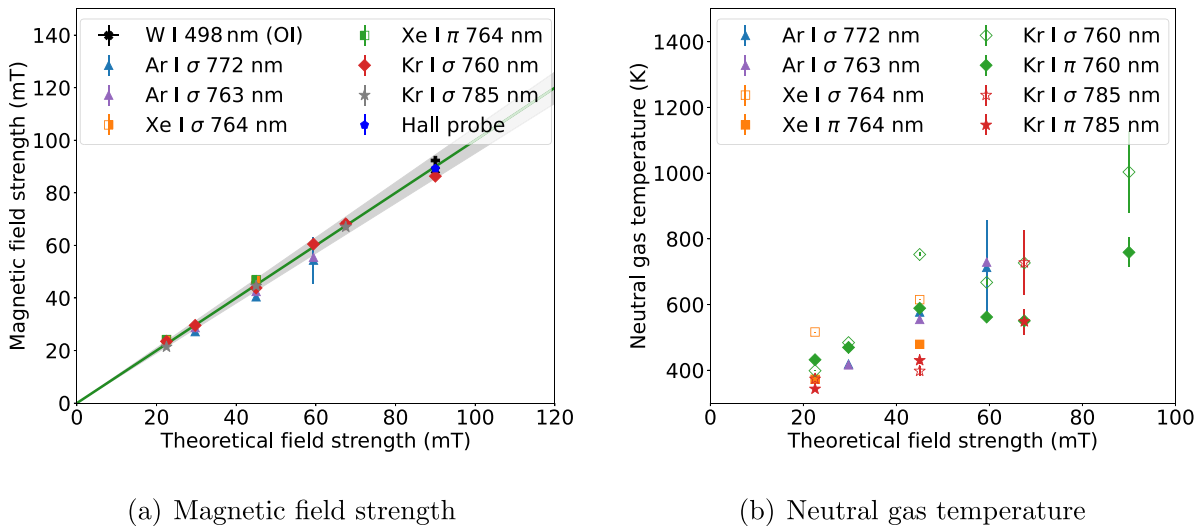
field than predicted [8]. Thus, it may be interesting to investigate a mixed Ar–Kr plasma to monitor whether this trend is reproducible. The final set of data points is from probing the magnetic field by optical isolation of emission of sputtered tungsten atoms, as discussed in detail in [58].

Figure 8(b) presents the neutral gas temperature obtained from the fits and shows similar behavior for all atomic species investigated via laser absorption at PSI-2. The discharge burned between a hollow ring-shaped cathode and anode at a fixed current of around 150 A. Varying the field strength changes the confinement of the plasma. Thus, the number of plasma particles leaving the source region increases when applying a higher magnetic field. The particles propagate into the exposure area accessible by the TDLAS system. Langmuir probe measurements of the plasma parameters verify this assumption, and having more charged particles distributing kinetic energy onto the background gas explains why the neutral gas temperature increases for higher magnetic fields.

The temperatures derived from measuring  $\sigma$  and  $\pi$  components exhibit a systematic difference. One reason could be the line-of-sight integration of the spectra along the inhomogeneous magnetic field. An estimation using the CRM developed in [8] indicates that the decrease in magnetic field strength in the line-of-sight effectively broadens the  $\sigma_+$  and  $\sigma_-$  components (cf section 9.5 of [8]). The opposite effect occurs for  $\pi$  components as the FWHM of the Zeeman splitting



**Figure 7.** Experimentally measured line profiles of the 764.4 nm Xe I line for magnetic fields of 22.5 mT and 45 mT compared to modeling. Experimental data for  $\pi$  (a), (c) and  $\sigma$  (b), (d) transitions measured using rotated linear polarizer are shown using black line. The color coding is identical to figures 5 and 6, with the exception that Xe has two odd-numbered isotopes. Line positions and intensities of even isotopes in the WFA are indicated by grey bars. Red- and blue-colored bars represent the values derived from the Hamiltonians (14) for  $^{129}\text{Xe}$  and  $^{131}\text{Xe}$ , respectively.



**Figure 8.** figure (a) presents the magnetic field strengths obtained from laser absorption (Ar [8], Kr, Xe), optical isolation (OI) of  $\sigma_{-/+}$  components from sputtered tungsten [58] and a Hall probe measurement of the vacuum field. The solid line is the vacuum magnetic field strength calculated using the Biot–Savart law with 95% confidence interval in grey. Figure (b) shows the neutral gas temperature during the discharge according to the fit of the absorption profiles.

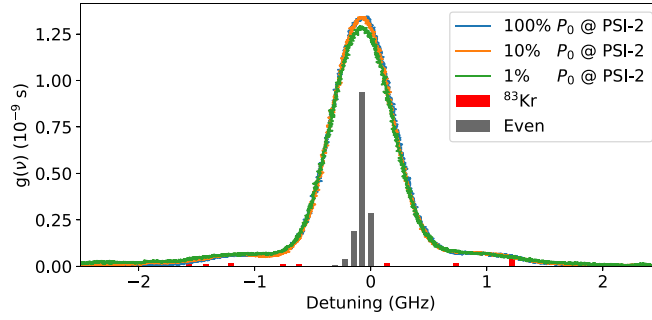


**Figure 9.** Line profile of the Kr I 760.4 nm transition measured at PSI-2 for a magnetic field of 22.5 mT while varying the photon flux density  $P_0$ . The bars indicate the zero field line positions and intensities of the even isotopes (grey) and  $^{83}\text{Kr}$  (red), as shown in figure 2(a). The blue-colored curve represents data acquired without attenuating the power (100%). Using two gray filters reduced the photon flux of the laser to 10% (orange) or 1% (green). The line profiles derived from the experimental data show only minor differences.

decreases. Therefore, the most accurate temperature is probably the average obtained from  $\pi$  and  $\sigma$  spectra. Using spectroscopic absorption tomography would avoid this problem. However, one has to consider a possible rotating component in the inverse Abel transform [59, 60]. Worth mentioning is also that linear plasma devices such as PSI-2 tend to develop instabilities, which could lead to a fluctuation of the neutral gas temperature within the machine [57, 61–63].

## 6. Saturation of Kr I 760.4 nm line

The probability of a transition absorbing a photon is linearly proportional to its oscillator strength. However, the density of the absorbing atomic state can drastically decrease as soon as absorption becomes comparable to the other depopulating collisional radiative processes. The oscillator strengths of hyperfine sub-transitions ( $f_{FF'}$ ) connect to the oscillator strength of their corresponding FS line ( $f_{JJ'}$ ) via [6]

$$f_{FF'} = (2F' + 1)(2J + 1) \left\{ \begin{array}{ccc} F & F' & 1 \\ J' & J & I \end{array} \right\}^2 f_{JJ'}, \quad (25)$$

while the sum rule [6]

$$\sum_{F'} f_{FF'} = f_{JJ'} \quad (26)$$

applies, which shows that the oscillator strength of hyperfine sub-transitions are smaller than those of the FS line ( $f_{FF'} < f_{JJ'}$ ). Thus, the laser depopulates the metastable density of even-numbered isotopes ( $f_{JJ'}$ ) significantly more than of the odd-numbered ones ( $f_{FF'}$ ). For instance, [21] presents zero-field simulations of the Xe I 834.9 nm for different saturation and exhibits precisely the above-described behavior. Consequently, the line profile of the 760.4 nm Kr I line should change if the laser perturbs the population density of the  $5s[3/2]_2^\circ$  level. To probe for saturation effects, we measured the laser absorption spectra of the Kr I 760.4 nm line at PSI-2 while varying the photon flux density over two orders of magnitude. These spectra do not demonstrate any line shape

changes, as figure 9 shows. This fact substantially simplifies the theoretical description of the spectra since each isotope contributes according to its natural abundance.

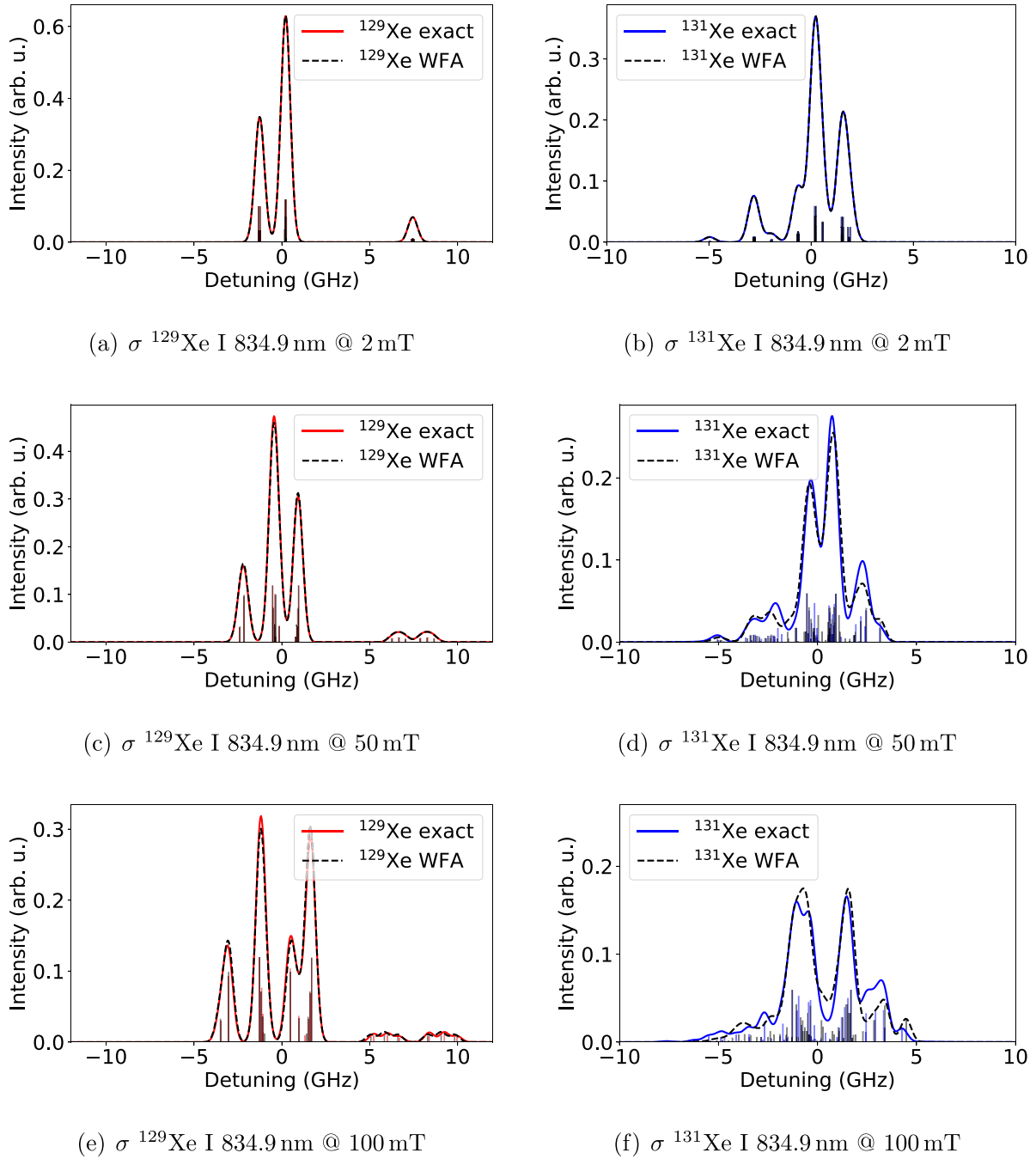
## 7. Modeling of the Xe I 834.9 nm line

The remarkable agreement of fit to experimental data, as seen in figures 5–7(a)–(d), validates the approach taken to investigate laser absorption spectra of odd-numbered isotopes at the intermediate field regime. Thus, it enables clearing up the commonly found inconsistency of analyzing LIF spectra in Xe thrusters.

Again, the approach is the same as before. One starts with the zero-field pattern of the Xe I 834.9 nm line, as shown in figure 3(b). Synthetic spectra by  $^{129}\text{Xe}$  and  $^{131}\text{Xe}$  of  $\sigma$  components, assuming a neutral gas temperature of 800 K observed in the experiment of [22], are shown in figures 10(a)–(f). Analyzing the Hamiltonians (14) for 2 mT, 50 mT, and 100 mT provides the energy eigenvalues and expansion coefficients used to calculate the frequency shifts and relative line intensities.

Figures 10(a) and (b) present the  $\sigma$  spectra of  $^{129}\text{Xe}$  and  $^{131}\text{Xe}$  calculated for 2 mT. In essence, the line shapes are identical when considering the exact or WFA standing in stark contrast to the finding at 1.7 mT reported in [23]. Our result matches quite well with the non-linear ZHFS model of [23] incorporating the results of Darwin [15] but shows significant differences compared to their weak field pattern (figure 14 of [23]).

Increasing the field to 50 mT does not give substantial line shape differences for the WFA and exact solution of  $^{129}\text{Xe}$ , but the spectra of  $^{131}\text{Xe}$  undoubtedly differ in their line shape. Our simulations also do not indicate a strong component of  $^{131}\text{Xe}$  at a detuning of 5 GHz, as suggested by [22] using the WFA. The difference between the WFA and exact calculations grows further for  $^{131}\text{Xe}$  at 100 mT. The profiles of the  $^{129}\text{Xe}$  isotope exhibit almost imperceptible differences in the line shape. Our simulations prove that the WFA works well in the case of  $^{129}\text{Xe}$  for fields up to 100 mT, but it breaks for  $^{131}\text{Xe}$  for magnetic

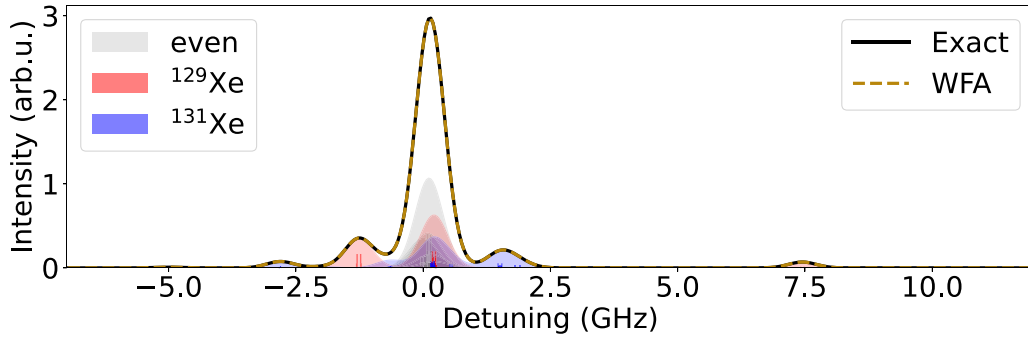
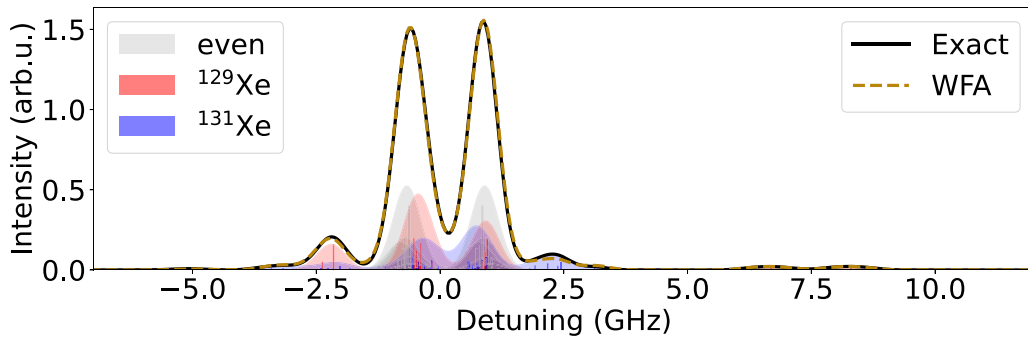
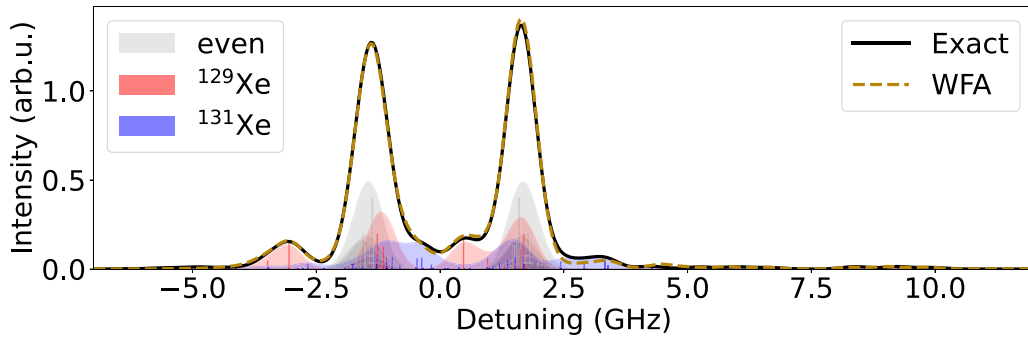


**Figure 10.** Spectra simulated for isolated  $\sigma$  components of odd-numbered Xe isotopes. The red and blue-colored bars indicate the line positions and intensities according to the evaluation of the Hamiltonians (14) for the 129 and 131 Xe isotopes, respectively—the exact approach. The grey-colored bars represent the line positions and intensities using the WFA formulas. The solid lines represent the exact solution, whereas the dashed lines are based on the WFA formulas. A neutral gas temperature of 800 K is assumed [22].

fields of a few tens of mT. At such fields, it becomes necessary to evaluate the Hamiltonians (14) when modeling the  $^{131}\text{Xe}$  I 834.9 nm transitions to correctly capture its line profile.

Figures 11(a)–(c) present the composite spectra that account for all isotopes, and the simulated Xe I 834.9 nm lines indicate better agreement between the WFA and exact

calculations compared to the transition at 764.4 nm. This behavior occurs since the hyperfine interaction constants associated with the 834.9 nm line are generally larger (cf tables 5 and 7). The difference between WFA and the exact solution for 834.9 nm exists practically only at the detuning frequencies dominated by the  $^{131}\text{Xe}$  isotope, as shown in figures 11(a)–(c).


 (a)  $\sigma$  Xe I 834.9 nm @ 2 mT

 (b)  $\sigma$  Xe I 834.9 nm @ 50 mT

 (c)  $\sigma$  Xe I 834.9 nm @ 100 mT

**Figure 11.** Isotopic contributions to the line shape by  $\sigma$  components of a commonly used line in LIF for measuring the velocity of the propellant. A neutral gas temperature of 800 K is assumed [22].

## 8. Conclusion

TDLAS provides, in this study, absorption spectra from metastable states of neutral krypton (760.4 nm, 785.7 nm) and xenon (764.4 nm) measured at the linear plasma device PSI-2 operating at a magnetic field of 22.5 mT–90 mT. Comparing the results with argon spectra [8] of similar types of transitions connected to metastable Ar states reveals additional complex structures for the Kr I and Xe I lines, which occur in both cases of isolated absorption by the  $\sigma$  ( $\Delta m = \pm 1$ ) and  $\pi$  ( $\Delta m = 0$ ) components. The isotopic composition and the interaction

of the magnetic moment of the nucleus of odd-numbered isotopes with the magnetic field are primarily responsible for the appearance of the detected structure. Accurately describing the absorption spectra consisting of contributions by various even- and odd-numbered isotopes influenced by an external magnetic field is the central purpose of this work.

Isotopic effects shift the energy of transitions, which is crucial for describing the absorption spectra of gases having various stable isotopes like Kr and Xe. The external magnetic field (<90 mT) generated by the six solenoids at PSI-2 provides weak field conditions for all even-numbered isotopes since it

induces an energy splitting, which is negligible compared to the FS splitting. Expressions (15)–(17) accurately reproduce the Zeeman pattern in this regime.

The situation regarding the odd-numbered isotopes of  $^{83}\text{Kr}$ ,  $^{129}\text{Xe}$ , and  $^{131}\text{Xe}$ , whose nuclei possess small magnetic momenta, is more challenging. Indeed, the magnetic moment associated with the core interacts with the valence electrons, which provides a magnetic dipole shift. This interaction creates the well-known HFS in the absence of external fields. However, the HFS splitting at magnetic fields of the PSI-2 is comparable to the splitting due to the external field (tables 6 and 7). Thus, using weak or strong field approximations is erroneous for describing the energies of transitions and intensities of magnetic components for the odd isotopes. Instead, the hyperfine interaction terms must be added to the Hamiltonian, which includes Zeeman terms. Using the basis of the uncoupled wavefunctions  $|Im_j Jm_j\rangle$  in the perturbative approach and the standard expressions of the step-up and down operators [49] enables calculating the matrix elements. Diagonalizing the obtained matrix provides the energy eigenvalues and expansion coefficients, which, inserted into equation (A.6), gives the relative intensities of hyperfine sub-components. Section 4.2.3 provides more details.

Accounting for all isotopes while fitting the absorption spectra gave an excellent agreement with the experimental data for the lines of Kr I (760.4 nm, 785.7 nm) and Xe I (764.4 nm). In particular, the magnetic field obtained from the optimization procedure matches remarkably well with the numerical calculations of the magnetic field in vacuum or other measurements, such as optical isolation of spectral lines. Interestingly, the Xe I spectra allow estimating the magnetic field from the  $\pi$  components enabled by the hyperfine interaction.

One of the principal problems raised in plasma technology, such as Hall-effect thrusters, is the validity of the WFA formulas (17) for magnetic fields of tens of mT. Strictly speaking, the calculations for the transitions of the  $^{83}\text{Kr}$  isotope exhibit a difference in the intensity distribution of components between the exact calculation and the WFA for the magnetic field of 22.5 mT and 45 mT. In our experiment, the Doppler broadening smooths the difference so that the transitions of  $^{83}\text{Kr}$  isotope at 760.4 nm and 785.7 nm appear as broad ‘wings’. Unfortunately, it is impossible to detect the deviations between the weak field and the exact calculations in the current experiment as the fraction of the odd isotope is quite low (11.5%) and the signal-to-noise ratio must be further improved.

For testing the atomic model, more favorable conditions exist in the case of Xe I transitions, as the fraction of odd isotopes in the gas is simply larger. For the magnetic field of 22.5 mT, the results of the WFA and the exact calculation match and describe the experimental spectra of  $\sigma$  and  $\pi$  components quite well. However, at the magnetic field of 45 mT, the situation changes. The experimental data can be described much better using the exact calculation. The profiles of  $^{129}\text{Xe}$  and  $^{131}\text{Xe}$  obtained using WFA, as shown in figures 4(c) and (d), fail to describe the experimental data in figures 7(c) and (d). We point out that the parameter  $\epsilon$ , being used as the merit of the application of the weak field results, has even lower values for the

upper levels of the Xe I lines compared to Kr I. Obviously, only the value  $\epsilon \ll 1$  guarantees the condition of the WFA. In the other cases, the weak field calculation could deviate from the exact calculations. Our comparison between Kr I and Xe I lines clearly underlines this.

The successful description of the Xe I 764.4 nm line at the linear plasma device PSI-2 prompted us to investigate the Xe I 834.9 nm line, which is frequently used for measuring the velocity of neutral xenon in hall thrusters. The results demonstrate the following. For the  $^{129}\text{Xe}$  isotope and magnetic fields below 100 mT, the WFA can be applied without limitation. In the case of  $^{131}\text{Xe}$ , the spectra at 2 mT are identical when using WFA formulas and the exact method. However, a considerable mixing of magnetic sublevels occurs for  $^{131}\text{Xe}$  at the fields of 50 mT. Thus, for this isotope, strictly speaking, WFA formulas do not apply for the fields above a few tens of mT (figure 10). Nevertheless, the larger values of the HFS constant for the upper and lower levels of the Xe I 834.9 nm line guarantee better agreement between the WFA and exact calculations compared to the transition at 764.4 nm. This fact explains why the composite spectra, including all isotopes of xenon, shown in figures 11(a)–(c), are very alike when using the WFA and the exact calculations. The difference exists only at the detuning frequencies dominated by the  $^{131}\text{Xe}$  isotope.

Comparing the results to the literature values shows that our spectra at 2 mT for the Xe I 834.9 nm line hardly agree with the data of [23]. In that work, the theoretical spectra produced assuming the WFA or using the model by Darwin [15] differ substantially at fields as low as 1.7 mT. Our results match closely with their non-linear ZHFS results. At the same time, we cannot confirm the weak field calculation of [22] at the detuning frequency of 5 GHz. Neither the WFA nor the exact solution demonstrates a strong  $^{131}\text{Xe}$  I line component at this position.

Measuring the TDLAS or LIF spectra of spectral lines of the pure isotopes  $^{83}\text{Kr}$ ,  $^{129}\text{Xe}$  or  $^{131}\text{Xe}$  will provide much deeper insight into the validity of the WFA at the field of tens of mT at the linear plasma device. At the same time, the newly developed model can be applied to distinguish the different isotopes of sputtered materials during plasma surface interaction. For instance, tungsten—one of the crucial materials in fusion research—has one odd-numbered isotope ( $^{183}\text{W}$ ) with a natural abundance of 14.3%, which may influence its line shape. We are going to address both problems in the near future.

## Data availability statement

All data that support the findings of this study are included within the article (and any supplementary files).

## Acknowledgment

We thank Evgeny Stambulchik and the anonymous reviewers for useful comments and valuable suggestions. This work has been carried out within the framework of the EUROfusion

Consortium, funded by the European Union via the Euratom Research and Training Programme (Grant Agreement No 101052200 – EUROfusion). Views and opinions expressed are however those of the author(s) only and do not necessarily reflect those of the European Union or the European Commission. Neither the European Union nor the European Commission can be held responsible for them.

### Appendix. Relative intensities of magnetic sub-transitions

The first-order perturbation theory approach provides the expansion coefficients  $\alpha$  needed to express the wave functions of the atomic states as

$$|\Psi_a\rangle = \sum_l \alpha_{a,l} |\Phi_l\rangle, \quad (\text{A.1})$$

with  $|\Phi_l\rangle$  the unperturbed wave function. The line strength of an electric dipole transition is then given by [6]

$$S_{ab} = |\langle \Psi_a | P_q^{(1)} | \Psi_b \rangle|^2 = \left| \sum_{l,l'} \alpha_{a,l} \alpha_{b,l'} \langle \Phi_l | P_q^{(1)} | \Phi_{l'} \rangle \right|^2, \quad (\text{A.2})$$

with  $P_q^{(1)}$  being the electric dipole operator. Next, the unperturbed wave function is described by a set of quantum numbers:

$$|\Phi_l\rangle = |\gamma I m_J J m_J\rangle, \quad (\text{A.3})$$

with  $\gamma$  containing all other quantum numbers, such as parity and principal quantum number. The Wigner–Eckart theorem [64, 65] and the fact that the E1 operator acts only upon the spatial components of the wave functions [6] simplify calculating the matrix elements of equation (A.2) to [66]

$$\begin{aligned} & \langle \gamma I m_J J m_J | P_{m_J - m_J'}^{(1)} | \gamma' I' m_J' J' m_J' \rangle \\ &= (-1)^{J - m_J} \times \begin{pmatrix} J & 1 & J' \\ -m_J & m_J - m_J' & m_J' \end{pmatrix} \\ & \langle \gamma J | P^{(1)} | \gamma' J' \rangle \langle I m_J || I' m_J' \rangle. \end{aligned} \quad (\text{A.4})$$

This equation contains the reduced matrix element  $\langle \gamma J | P^{(1)} | \gamma' J' \rangle$ , which depends on the wave functions without the hyperfine and Zeeman interaction. As such, the reduced matrix element is a constant and is available in the literature for the Kr I and Xe I transitions considered in this work. The term  $\langle I m_J || I' m_J' \rangle$  is only nonzero if the quantum numbers are the same since these wave functions span an orthonormal basis, providing us with the selection rule of

$$\Delta m_J = 0. \quad (\text{A.5})$$

Combining all of the above equations yields the line strength

$$S_{ab} \propto \left| \sum_{l,l'} \alpha_{a,l} \alpha_{b,l'} (-1)^{J_l - m_{J_l}} \begin{pmatrix} J_l & 1 & J_{l'} \\ -m_{J_l} & m_{J_l} - m_{J_{l'}} & m_{J_{l'}} \end{pmatrix} \right|^2, \quad (\text{A.6})$$

which is linearly proportional to the intensity [49].

### ORCID iDs

M Sackers [id https://orcid.org/0000-0002-5106-3373](https://orcid.org/0000-0002-5106-3373)  
 O Marchuk [id https://orcid.org/0000-0001-6272-2605](https://orcid.org/0000-0001-6272-2605)  
 D Dipti [id https://orcid.org/0000-0001-6675-8509](https://orcid.org/0000-0001-6675-8509)  
 Yu Ralchenko [id https://orcid.org/0000-0003-0083-9554](https://orcid.org/0000-0003-0083-9554)  
 S Ertmer [id https://orcid.org/0000-0002-8978-9567](https://orcid.org/0000-0002-8978-9567)  
 S Brezinsek [id https://orcid.org/0000-0002-7213-3326](https://orcid.org/0000-0002-7213-3326)  
 A Kreter [id https://orcid.org/0000-0003-3886-1415](https://orcid.org/0000-0003-3886-1415)

### References

- [1] Shikama T, Fujii M, Mizushiri K, Hasuo M, Kado S and Zushi H 2009 Calculation of a magnetic field effect on emission spectra of light diatomic molecules for diagnostic application to fusion edge plasmas *Plasma Phys. Control. Fusion* **51** 122001
- [2] Tessarin S et al 2011 Beyond Zeeman spectroscopy: magnetic-field diagnostics with Stark-dominated line shapes *Phys. Plasmas* **18** 093301
- [3] Dickheuer S, Marchuk O, Tsankov Ts V, Luggenhölscher D, Czarnetzki U, Gromelski W, Ertmer S and Kreter A 2019 Measurement of the magnetic field in a linear magnetized plasma by tunable diode laser absorption spectroscopy *Atoms* **7** 48
- [4] Bergert R and Mitic S 2019 Optical properties of magnetized transient low-pressure plasma *Plasma Sources Sci. Technol.* **28** 115001
- [5] Barman K, Mudgal M, Rane R and Bhattacharjee S 2021 Effect of magnetic field on optical emission from cold atmospheric pressure micro-plasma jet *Phys. Plasmas* **28** 241501
- [6] Cowan R D 1981 *The Theory of Atomic Structure and Spectra (Los Alamos Series in Basic and Applied Sciences vol 3)* (University of California Press)
- [7] Weaver J L, Welch B L, Griem H R, Terry J, Lipschultz B, Pitcher C S, Wolfe S, Pappas D A and Boswell C 2000 Localization of emission through interpretation of observed Zeeman pattern *Rev. Sci. Instrum.* **71** 1664–70
- [8] Sackers M, Marchuk O, Ertmer S, Dickheuer S, Czarnetzki U, Tsankov Ts V, Luggenhölscher D, Brezinsek S and Kreter A 2021 Zeeman-resolved TDLAS using metastable levels of Ar in the weakly magnetized plasma of the linear plasma device PSI-2 *J. Phys. D: Appl. Phys.* **54** 395001
- [9] Wimmer C, Lindauer M and Fantz U 2018 Determination of the Cs distribution along a line of sight by the Zeeman splitting in an inhomogeneous magnetic field *J. Phys. D: Appl. Phys.* **51** 395203
- [10] Windholz L and Musso M 1988 Zeeman- and Paschen-Back-effect of the hyperfine structure of the sodium D 2-line *Eur. Phys. J. D* **8** 239–49
- [11] Tremblay P, Michaud A, Levesque M, Thériault S, Breton M, Beaubien J and Cyr N 1990 Absorption profiles of alkali-metal D lines in the presence of a static magnetic field *Phys. Rev. A* **42** 2766–73

- [12] Zentile M A, Keaveney J, Weller L, Whiting D J, Adams C S and Hughes I G 2015 ElecSus: a program to calculate the electric susceptibility of an atomic ensemble *Comput. Phys. Commun.* **189** 162–74
- [13] Froese Fischer C, Gaigalas G, Jönsson P and Bieroń J 2019 GRASP2018—A Fortran 95 version of the General Relativistic Atomic Structure Package *Comput. Phys. Commun.* **237** 184–7
- [14] Li W, Grumer J, Brage T and Jönsson P 2020 Hfszeeman95—A program for computing weak and intermediate magnetic-field- and hyperfine-induced transition rates *Comput. Phys. Commun.* **253** 107211
- [15] Darwin C G 1927 The Zeeman effect and spherical harmonics *Proc. R. Soc. A* **115** 1–19
- [16] Goudsmit S and Bacher R F 1929 The Paschen-Back effect of hyperfine structure *Phys. Rev.* **34** 1499–500
- [17] Tirila V-G, Demairé A and Ryan C N 2023 Review of alternative propellants in Hall thrusters *Acta Astronaut.* **212** 284–306
- [18] Hargus W 2010 A Preliminary Study of Krypton Laser-Induced Fluorescence *46th AIAA/ASME/SAE/ASEE Joint Propulsion Conf. & Exhibit* (American Institute of Aeronautics and Astronautics) (<https://doi.org/10.2514/6.2010-6524>)
- [19] Mazouffre S, Kulaev V and Luna J P 2009 Ion diagnostics of a discharge in crossed electric and magnetic fields for electric propulsion *Plasma Sources Sci. Technol.* **18** 034022
- [20] Svarnas P, Romadanov I, Diallo A and Raitses Y 2018 Laser-Induced Fluorescence of Xe I and Xe II in ambipolar plasma flow *IEEE Trans. Plasma Sci.* **46** 3998–4009
- [21] Pietzonka L, Eichhorn C, Scholze F and Spemann D 2023 Laser-induced fluorescence spectroscopy for kinetic temperature measurement of xenon neutrals and ions in the discharge chamber of a radiofrequency ion source *J. Electr. Propuls.* **2** 4
- [22] Vinci A E, Mazouffre S, Gómez V, Fajardo P and Navarro-Cavallé J 2022 Laser-induced fluorescence spectroscopy on xenon atoms and ions in the magnetic nozzle of a helicon plasma thruster *Plasma Sources Sci. Technol.* **31** 095007
- [23] Ngom B B, Smith T B, Huang W and Gallimore A D 2008 Numerical simulation of the Zeeman effect in neutral xenon from NIR diode-laser spectroscopy *J. Appl. Phys.* **104** 023303
- [24] Hargus W, Azarnia M and Nakles M 2011 Demonstration of laser-induced fluorescence on krypton Hall effect thruster *Proc. 32nd Int. Electric Propulsion Conf. (Wiesbaden)* 2011-018
- [25] Kreter A, Brandt C, Huber A, Kraus S, Möller S, Reinhart M, Schweer B, Sergienko G and Unterberg B 2015 Linear plasma device PSI-2 for plasma-material interaction studies *Fusion Sci. Technol.* **68** 8–14
- [26] Kramida A and Yu Ralchenko J R (NIST ASD Team) 1999 NIST Atomic Spectra Database, NIST Standard Reference Database 78 (<https://doi.org/10.18434/T4W30F>)
- [27] Sugar J and Musgrove A 1991 Energy levels of krypton, Kr I through Kr XXXVI *J. Phys. Chem. Ref. Data* **20** 859–915
- [28] Safia H A, Grandin J P and Husson X 1981 g factor measurements for Ne, Ar and Kr *J. Phys. B: At. Mol. Phys.* **14** 3363–8
- [29] Husson X and Grandin J P 1979 Measurements of g factors of Xe and Kr *J. Phys. B: At. Mol. Phys.* **12** 3649–53
- [30] Humphreys C J and Paul E 1970 Interferometric Wavelength Determinations in the First Spectrum of  $^{136}\text{Xe}$  *J. Opt. Soc. Am.* **60** 1302
- [31] Sadeghi N 2004 6. Molecular spectroscopy techniques applied for processing plasma diagnostics *J. Plasma Fusion Res.* **80** 767–76
- [32] Niermann B, Böke M, Sadeghi N and Winter J 2010 Space resolved density measurements of argon and helium metastable atoms in radio-frequency generated He-Ar micro-plasmas *Eur. Phys. J. D* **60** 489–95
- [33] Fujimoto T 2004 *Plasma Spectroscopy (International Series of Monographs on Physics vol 123)*
- [34] Corney A 1979 *Atomic and Laser Spectroscopy* (Oxford Science Publications) (Clarendon [u.a.]) 1st publ. in paperback edition
- [35] Fisher V, Bernshtam V, Golten H and Maron Y 1996 Electron-impact excitation cross sections for allowed transitions in atoms *Phys. Rev. A* **53** 2425–32
- [36] Griem H R 1968 Semiempirical formulas for the electron-impact widths and shifts of isolated ion lines in plasmas *Phys. Rev.* **165** 258–66
- [37] King W H 1984 *Isotope Shifts in Atomic Spectra Physics of Atoms and Molecules* (Plenum Press)
- [38] Cannon B D and Janik G R 1990 Hyperfine splittings and isotope shifts in eight transitions from the metastable  $4p^5\ 5s\ J = 2$  and  $J = 0$  states of Kr I *Phys. Rev. A* **42** 397–402
- [39] Jackson D A 1974 Isotope shifts in the arc spectrum of xenon *Proc. R. Soc. A* **338** 277–98
- [40] Suzuki M, Katoh K and Nishimiya N 2002 Saturated absorption spectroscopy of Xe using a GaAs semiconductor laser *Spectrochim. Acta A* **58** 2519–31
- [41] Audi G, Bersillon O, Blachot J and Wapstra A H 2003 The Nubase evaluation of nuclear and decay properties *Nucl. Phys. A* **729** 3–128
- [42] Kopfermann H and Schneider E E 1958 *Nuclear Moments (Pure and Applied Physics vol 2)* (Academic)
- [43] Woodgate G K 1992 *Elementary Atomic Structure* 2nd reprinted. edn (Clarendon)
- [44] Casimir H B G 1936 *On the Interaction Between Atomic Nuclei and Electrons* (Springer)
- [45] Jaccarino V, King J G, Satten R A and Stroke H H 1954 Hyperfine structure of  $\text{I}127$ . Nuclear magnetic octupole moment *Phys. Rev.* **94** 1798–9
- [46] Schwartz C 1955 Theory of hyperfine structure *Phys. Rev.* **97** 380–95
- [47] Becker O, Enders K, Werth G and Dembczynski J 1993 Hyperfine-structure measurements of the  $151,153\text{Eu}^+$  ground state *Phys. Rev. A* **48** 3546–54
- [48] G Drake (ed) 2006 *Springer Handbook of Atomic, Molecular and Optical Physics: With 111 tables* Neuaufld edn (Springer)
- [49] Condon E U and Shortley G 1979 *The Theory of Atomic Spectra* reprinted. edn (University Press)
- [50] Cannon B D 1993 Hyperfine spectra of the radioactive isotopes Kr81 and Kr85 *Phys. Rev. A* **47** 1148–58
- [51] D'Amico D, Pesce G and Sasso A 1999 Isotope-shift and hyperfine-constant measurements of near-infrared xenon transitions in glow discharges and on a metastable  $\text{Xe}(3P_2)$  beam *Phys. Rev. A* **60** 4409–16
- [52] Garstang R H 1977 Atoms in high magnetic fields (white dwarfs) *Rep. Prog. Phys.* **40** 105–54
- [53] Stone N J 2019 Table of recommended nuclear magnetic dipole moments (INDC(NDS)–0794) International Atomic Energy Agency (IAEA) (<https://doi.org/10.61092/iaea.yjpc-cns6>)
- [54] Goudsmit S and Bacher R F 1930 Der Paschen-Back-Effekt der Hyperfeinstruktur *Z. Phys.* **66** 13–30
- [55] Steck D A 2007 *Quantum and Atom Optics* (available at: <http://steck.us/teaching>)
- [56] Jackson D A and Kuhn H 1938 The hyperfine structure of the Zeeman components of the resonance lines of sodium *Proc. R. Soc. A* **167** 205–16
- [57] Klose S 2000 Untersuchung der Driftinstabilität an der Rotierenden Magnetisierenden Plasmasäule des PSI-1 im Falle eines Plasmahohlprofils und großer Endlicher

- Ionengyoradieneffekte *PhD Thesis* Humboldt-Universität zu, Mathematisch-Naturwissenschaftliche Fakultät I
- [58] Ertmer S, Marchuk O, Sackers M, Dickheuer S, Brezinsek S, Mertens P and Kreter A 2020 Optical isolation of spectral lines emitted by sputtered tungsten in a weakly magnetized plasma *J. Phys. B: At. Mol. Opt. Phys.* **54** 025401
- [59] Fussmann G, Meyer H and Pasch E 1996 Abel inversion of rotating plasmas *Contrib. Plasma Phys.* **36** 501–17
- [60] Waldmann O, Meyer H and Fussmann G 2007 Anomalous diffusion in a linear plasma generator *Contrib. Plasma Phys.* **47** 691–702
- [61] Horton W 1999 Drift waves and transport *Rev. Mod. Phys.* **71** 735–78
- [62] Grulke O and Klinger T 2002 Large-scale fluctuation structures in plasma turbulence *New J. Phys.* **4** 67
- [63] Thakur S C, Brandt C, Cui L, Gosselin J J, Light A D and Tynan G R 2014 Multi-instability plasma dynamics during the route to fully developed turbulence in a helicon plasma *Plasma Sources Sci. Technol.* **23** 044006
- [64] Wigner E 1927 Einige folgerungen aus der schrödingerschen theorie für die termstrukturen *Z. Phys.* **43** 624–52
- [65] Eckart C 1930 The application of group theory to the quantum dynamics of monatomic systems *Rev. Mod. Phys.* **2** 305–80
- [66] Sobelman I I 1992 *Atomic Spectra and Radiative Transitions* (Springer)